

Ultralow-Frequency Geomagnetic Signal Estimation: An Interstation Transfer Function Method Based on Multivariate Wavelet Coherence

Hongyan Chen, Peng Han^{ID}, Member, IEEE, and Katsumi Hattori^{ID}, Member, IEEE

Abstract—Electromagnetic perturbations associated with earthquakes and volcano eruptions have been intensively documented in the past decades, from both ground and satellite observations. However, the magnetic signals associated with crustal activity are usually very weak and mixed with global geomagnetic signals originating from external sources. Thus, one of the key issues in seismo-electromagnetic study is to identify local geomagnetic signals from global magnetic pulsations. The interstation transfer function can recover the global magnetic pulsations at the observatory by using the data of reference station, providing an effective way for signal discrimination. To further improve the accuracy of global magnetic signal estimation, in this study, we develop a new method for interstation transfer function calculation based on multivariate wavelet coherence using adaptive selection of time window lengths for different periods. Test on real data demonstrates that the global signals of the external source are accurately estimated, including the horizontal X and Y components and the vertical Z component of the observatory. The results of using different reference stations confirm the robustness of the proposed method. It is proved that the method can be used to eliminate the external ionospheric source signals effectively and identify local magnetic field signals lying in the background at the observatory. The proposed method can be useful in seismo-electromagnetic signal identification and extraction.

Index Terms—Interstation transfer function, multivariate wavelet coherence, ultralow-frequency (ULF) geomagnetic signal estimation.

I. INTRODUCTION

ELectromagnetic perturbations associated with earthquakes and volcano eruptions have been intensively

Received 3 April 2024; revised 29 July 2024; accepted 23 August 2024. Date of publication 9 September 2024; date of current version 24 September 2024. This work was supported in part by the National Key Research and Development Program of China under Grant 2023YFE0101800, in part by the National Natural Science Foundation of China under Grant 42222405, in part by Guangdong Provincial Key Laboratory of Geophysical High-Resolution Imaging Technology under Grant 2022B1212010002, in part by China Postdoctoral Science Foundation under Grant 2024M751293, and in part by the Ministry of Education, Culture, Sports, Science and Technology (MEXT) of Japan under Grant CBA_01. (Corresponding author: Peng Han.)

Hongyan Chen and Peng Han are with Guangdong Provincial Key Laboratory of Geophysical High-Resolution Imaging Technology, Department of Earth and Space Sciences, Southern University of Science and Technology, Shenzhen 518055, China (e-mail: chenhy@sustech.edu.cn; hanp@sustech.edu.cn).

Katsumi Hattori is with the Graduate School of Science and the Center for Environmental Remote Sensing, Chiba University, Chiba 263-8522, Japan (e-mail: khattori@faculty.chiba-u.jp).

The interstation transfer function calculation method in the study is available online at <https://github.com/hongyanch/Transfer-function>.

Digital Object Identifier 10.1109/TGRS.2024.3456433

documented in the past decades, from both ground and satellite observations [1], [2], [3], [4], [5], [6], [7], [8], [9], [10], [11], [12], [13], [14], [15], [16], [17], [18], [19]. The ultralow-frequency geomagnetic signals (less than 1 Hz) in the lithosphere have attracted widespread attention in the study of seismo-electromagnetism [20], [21], [22], [23], [24], [25], [26], [27], [28], [29], [30], because of their deeper skin depths. However, the geomagnetic signals associated with crustal activity could be very weak. They are usually mixed with external field resources, including natural global signals, such as daily variations of the geomagnetic field, magnetic pulsations, and regional artificial noises [31]. Therefore, the key is how to extract the geomagnetic signals from other noises [16]. In previous study, the data only in the midnight time were used because the artificial noises are considered to be much less than those in the daytime. On this basis, extracting the signals from the global natural signals is the most important thing.

Scholars have proposed some analytical methods, such as polarization analysis [22], [32], fractal analysis [33], principal component analysis [23], [34], and machine learning methods [35], [36], [37]. Recently, QuakeFinder and Google used artificial intelligence method to improve the efficiency and accuracy of electromagnetic anomaly detection [16] but did not include removal of external sources and extraction of waveforms. Harada et al. [31] proposed the interstation transfer function method, which can establish the relationship between the observatory and the reference station, to recover the change of the natural background signal of the observatory. However, the window lengths for different period signals in the previous method were too rough to be divided, and multivariate coherent calculation accuracy was limited, resulting in low calculation accuracy and stability for interstation transfer function, which can be further improved. In this article, we develop a new method based on multivariate wavelet coherence, to improve the accuracy of interstation transfer function. We apply it to extract local geomagnetic signals from the external source signals. Test on real data demonstrates the effectiveness of estimating the global geomagnetic signals and confirms the robustness of the proposed method. The method proposed in the current work may have some potential applications in seismo-electromagnetic signal identification and extraction.

II. METHODS

A. Interstation Transfer Function Method

The interstation transfer function is defined by the following formula [31]:

$$\begin{pmatrix} \Delta X_s(\omega) \\ \Delta Y_s(\omega) \\ \Delta Z_s(\omega) \end{pmatrix} = \begin{pmatrix} T_{xx}(\omega) & T_{xy}(\omega) \\ T_{yx}(\omega) & T_{yy}(\omega) \\ T_{zx}(\omega) & T_{zy}(\omega) \end{pmatrix} \begin{pmatrix} \Delta X_r(\omega) \\ \Delta Y_r(\omega) \end{pmatrix} \quad (1)$$

where $T_{xx}(\omega)$, $T_{xy}(\omega)$, $T_{yx}(\omega)$, $T_{yy}(\omega)$, $T_{zx}(\omega)$, and $T_{zy}(\omega)$ are interstation transfer functions between the observatory and the reference station. Suffixes s means the observed signal at the observatory and r means the signal at the reference station. $\Delta X_s(\omega)$, $\Delta Y_s(\omega)$, and $\Delta Z_s(\omega)$ are geographic NS, EW, and vertical components of geomagnetic variations in the observatory, respectively, and $\Delta X_r(\omega)$ and $\Delta Y_r(\omega)$ are the NS and EW components in the reference station, respectively. Through the six interstation transfer functions, the three components of the observatory can be represented by the horizontal components of the reference station

$$\Delta X_s(\omega) = T_{xx}(\omega) \cdot \Delta X_r(\omega) + T_{xy}(\omega) \cdot \Delta Y_r(\omega) \quad (2)$$

$$\Delta Y_s(\omega) = T_{yx}(\omega) \cdot \Delta X_r(\omega) + T_{yy}(\omega) \cdot \Delta Y_r(\omega) \quad (3)$$

$$\Delta Z_s(\omega) = T_{zx}(\omega) \cdot \Delta X_r(\omega) + T_{zy}(\omega) \cdot \Delta Y_r(\omega). \quad (4)$$

The essence of the interstation transfer function is the frequency response of a system. Based on the calculation method of system frequency response, the transfer function can be obtained by calculating the power spectrum of each component at the reference station and the observatory. A traditional approach involves the use of high-pass filters and Hanning windows, which are used to compute the self-power spectrum and cross-power spectrum for each data segment by employing the Fourier transform [38]. Subsequently, the transfer function values can be obtained by smoothing the frequency domain. However, when using the frequency-domain method for calculating the transfer function, some signals may appear for a short time, and this can be problematic [31]. In comparison to the frequency-domain approach, incorporating time-dimension information into the interstation transfer function calculation becomes advantageous. In the wavelet time–frequency domain, the transfer functions for period j at the moment t are expressed as follows [31]: (5)–(10), as shown at the bottom of the next page,

A time window is selected to calculate for each moment t . δ is the window length and T is the total length of the time series. $t - (\delta/2)$ and $t + (\delta/2)$ are the beginning and the end for one window, respectively. The moments that can be calculated range from $(\delta/2)$ to $T - (\delta/2)$. $WC_{\Delta X_r^j \Delta X_s^j}(\tau)$ can be expressed as follows:

$$WC_{\Delta X_r^j \Delta X_s^j}(\tau) = \Delta X_r^j(\tau)^* \cdot \Delta X_s^j(\tau) \quad (11)$$

where $\Delta X_s^j(\tau)$ is the wavelet coefficient of $\Delta X_s(t)$ at period j and time τ and $\Delta X_r^j(\tau)^*$ is the conjugate of wavelet coefficients of $\Delta X_r(t)$ at period j and time τ . The wavelet

coefficient of signal ΔX_r at τ moment can be calculated as follows:

$$\Delta X_r(a, \tau) = \frac{1}{\sqrt{a}} \int_{-\infty}^{+\infty} \Delta X_r(t) \Psi^* \left(\frac{t - \tau}{a} \right) dt, \quad (a > 0) \quad (12)$$

where a is the scale parameter, τ is different times, Ψ is the Morlet wavelet used in this study, and $*$ is the complex conjugate.

The period j ($1/f$) corresponding to the scale a can be obtained by the center frequency f_0 of Morlet wavelet, $f = f_0/a$. We take the mean value of all windows with high multivariate coherence as the final transfer function values corresponding to this period, including the complex part and the real part. The detailed calculation of multivariate coherence is illustrated in Section II-B. The calculated interstation transfer function results are described as T_{xx}^j , T_{xy}^j , T_{yx}^j , T_{yy}^j , T_{zx}^j , and T_{zy}^j . Then, we use the obtained interstation transfer function results of different frequencies (periods) to recover the global magnetic pulsations at the observatory. First, the time series $\Delta X_r(t)$ of the horizontal X component and $\Delta Y_r(t)$ of the Y component at the reference station are transformed into wavelet domain as $\Delta X_r^j(\tau)$ and $\Delta Y_r^j(\tau)$, respectively. Then, the estimated three components of the observatory are obtained in the wavelet domain according to the interstation transfer function, as shown in (13)–(15), which is similar to those in (2)–(4)

$$\Delta X_{sre}^j(\tau) = T_{xx}^j \cdot \Delta X_r^j(\tau) + T_{xy}^j \cdot \Delta Y_r^j(\tau) \quad (13)$$

$$\Delta Y_{sre}^j(\tau) = T_{yx}^j \cdot \Delta X_r^j(\tau) + T_{yy}^j \cdot \Delta Y_r^j(\tau) \quad (14)$$

$$\Delta Z_{sre}^j(\tau) = T_{zx}^j \cdot \Delta X_r^j(\tau) + T_{zy}^j \cdot \Delta Y_r^j(\tau). \quad (15)$$

Finally, they are inversely transformed into a time domain to get the estimated values of the three components at the observatory. The flowchart of the study is shown in Fig. 1.

Usually, a different window length (δ) is simply set for different periods. In order to obtain more precise and accurate transfer function results, this study sets the window length as an exponential function related to the period (Fig. 2). In the high-frequency part, the window length is about five times the period, while the window length is the same as the corresponding period in the low-frequency part. The window movement step is 1 s. By the method, we realize the adaptive selection of the time window length for different periodic transfer functions' calculation and can get more sample data.

B. Multivariate Wavelet Coherence

Since there may be noise mixed in the original data signal, the calculated transfer function can be affected by the noise. It is necessary to calculate the coherence of the data and select the result of the window with a high coherence to obtain a more accurate transfer function. The multivariate wavelet coherence was first used in the application of climatic study, which helps diagnose the time series in a time–frequency domain [39]. Therefore, in this study, we introduce a strict multivariate coherence analysis method for interstation transfer function computation, which can analyze the relationship between each component of the observatory and the two

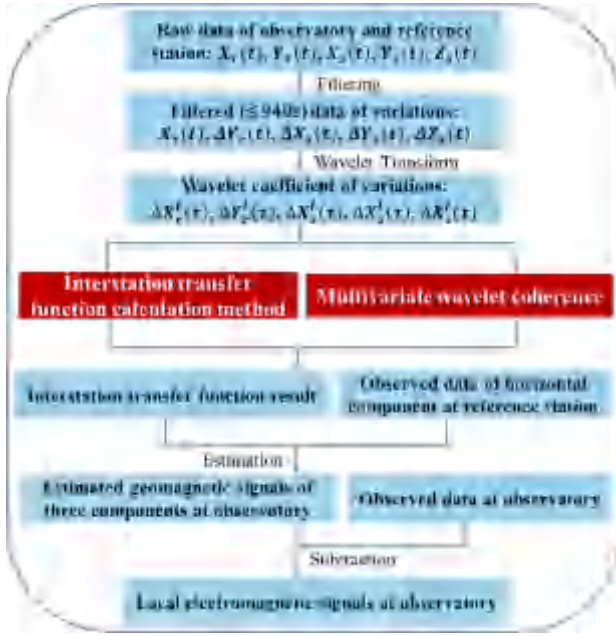


Fig. 1. Framework of the method used in the study.

horizontal components of the reference station. Taking the multivariate coherence analysis of ΔX_s with ΔX_r and ΔY_r as an example, the equation for calculating the multivariate coherence coefficient is given as follows [39]:

$R_{(\Delta X_s, \Delta X_r, \Delta Y_r)}^2(t, f)$ is the multivariate wavelet coherence coefficient between the X component of the observatory and the horizontal components of the reference station. Its value ranges from 0 to 1. The magnitude of $R_{(\Delta X_s, \Delta X_r, \Delta Y_r)}^2(t, f)$ represents the extent to which ΔX_s can be explained by the two

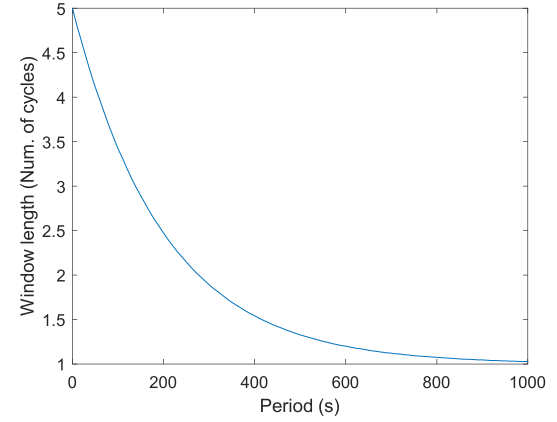


Fig. 2. Map of window lengths for different periods.

independent components ΔX_r and ΔY_r , at a given moment t and frequency f . When calculating the transfer functions, it is necessary to select the data with a high enough multivariate coherence coefficient to get a more accurate result. In (16), as shown at the bottom of the next page, $R_{\Delta X_s, \Delta X_r}^2(t, f)$ is the multivariate wavelet coherence coefficient between ΔX_s and ΔX_r , and the other items are similar. The mark * denotes conjugate. The formula expression of $R_{\Delta X_s, \Delta X_r}^2(t, f)$, $R_{\Delta X_s, \Delta Y_r}^2(t, f)$, and $R_{\Delta X_r, \Delta Y_r}^2(t, f)$ is given as follows [39]:

$$R_{(\Delta X_s, \Delta X_r)}^2(t, f) = R_{\Delta X_s, \Delta X_r}(t, f) \cdot R_{\Delta X_s, \Delta X_r}^*(t, f) \quad (17)$$

$$R_{(\Delta X_s, \Delta Y_r)}^2(t, f) = R_{\Delta X_s, \Delta Y_r}(t, f) \cdot R_{\Delta X_s, \Delta Y_r}^*(t, f) \quad (18)$$

$$R_{(\Delta X_r, \Delta Y_r)}^2(t, f) = R_{\Delta X_r, \Delta Y_r}(t, f) \cdot R_{\Delta X_r, \Delta Y_r}^*(t, f) \quad (19)$$

$$T_{xx}^j(t) = \frac{\int_{t-\frac{\delta}{2}}^{t+\frac{\delta}{2}} WC_{\Delta X_r^j \Delta X_s^j}(\tau) d\tau \cdot \int_{t-\frac{\delta}{2}}^{t+\frac{\delta}{2}} WC_{\Delta Y_r^j \Delta Y_r^j}(\tau) d\tau - \int_{t-\frac{\delta}{2}}^{t+\frac{\delta}{2}} WC_{\Delta X_r^j \Delta Y_r^j}(\tau) d\tau \cdot \int_{t-\frac{\delta}{2}}^{t+\frac{\delta}{2}} WC_{\Delta Y_r^j \Delta X_s^j}(\tau) d\tau}{\int_{t-\frac{\delta}{2}}^{t+\frac{\delta}{2}} WC_{\Delta X_r^j \Delta X_r^j}(\tau) d\tau \cdot \int_{t-\frac{\delta}{2}}^{t+\frac{\delta}{2}} WC_{\Delta Y_r^j \Delta Y_r^j}(\tau) d\tau - \left| \int_{t-\frac{\delta}{2}}^{t+\frac{\delta}{2}} WC_{\Delta X_r^j \Delta Y_r^j}(\tau) d\tau \right|^2} \quad (5)$$

$$T_{xy}^j(t) = \frac{\int_{t-\frac{\delta}{2}}^{t+\frac{\delta}{2}} WC_{\Delta Y_r^j \Delta X_s^j}(\tau) d\tau \cdot \int_{t-\frac{\delta}{2}}^{t+\frac{\delta}{2}} WC_{\Delta X_r^j \Delta X_r^j}(\tau) d\tau - \int_{t-\frac{\delta}{2}}^{t+\frac{\delta}{2}} WC_{\Delta Y_r^j \Delta X_r^j}(\tau) d\tau \cdot \int_{t-\frac{\delta}{2}}^{t+\frac{\delta}{2}} WC_{\Delta X_r^j \Delta X_s^j}(\tau) d\tau}{\int_{t-\frac{\delta}{2}}^{t+\frac{\delta}{2}} WC_{\Delta X_r^j \Delta X_r^j}(\tau) d\tau \cdot \int_{t-\frac{\delta}{2}}^{t+\frac{\delta}{2}} WC_{\Delta Y_r^j \Delta Y_r^j}(\tau) d\tau - \left| \int_{t-\frac{\delta}{2}}^{t+\frac{\delta}{2}} WC_{\Delta X_r^j \Delta Y_r^j}(\tau) d\tau \right|^2} \quad (6)$$

$$T_{yx}^j(t) = \frac{\int_{t-\frac{\delta}{2}}^{t+\frac{\delta}{2}} WC_{\Delta X_r^j \Delta Y_s^j}(\tau) d\tau \cdot \int_{t-\frac{\delta}{2}}^{t+\frac{\delta}{2}} WC_{\Delta Y_r^j \Delta Y_r^j}(\tau) d\tau - \int_{t-\frac{\delta}{2}}^{t+\frac{\delta}{2}} WC_{\Delta X_r^j \Delta Y_r^j}(\tau) d\tau \cdot \int_{t-\frac{\delta}{2}}^{t+\frac{\delta}{2}} WC_{\Delta Y_r^j \Delta Y_s^j}(\tau) d\tau}{\int_{t-\frac{\delta}{2}}^{t+\frac{\delta}{2}} WC_{\Delta X_r^j \Delta X_r^j}(\tau) d\tau \cdot \int_{t-\frac{\delta}{2}}^{t+\frac{\delta}{2}} WC_{\Delta Y_r^j \Delta Y_r^j}(\tau) d\tau - \left| \int_{t-\frac{\delta}{2}}^{t+\frac{\delta}{2}} WC_{\Delta X_r^j \Delta Y_r^j}(\tau) d\tau \right|^2} \quad (7)$$

$$T_{yy}^j(t) = \frac{\int_{t-\frac{\delta}{2}}^{t+\frac{\delta}{2}} WC_{\Delta Y_r^j \Delta Y_s^j}(\tau) d\tau \cdot \int_{t-\frac{\delta}{2}}^{t+\frac{\delta}{2}} WC_{\Delta X_r^j \Delta X_r^j}(\tau) d\tau - \int_{t-\frac{\delta}{2}}^{t+\frac{\delta}{2}} WC_{\Delta Y_r^j \Delta X_r^j}(\tau) d\tau \cdot \int_{t-\frac{\delta}{2}}^{t+\frac{\delta}{2}} WC_{\Delta X_r^j \Delta Y_s^j}(\tau) d\tau}{\int_{t-\frac{\delta}{2}}^{t+\frac{\delta}{2}} WC_{\Delta X_r^j \Delta X_r^j}(\tau) d\tau \cdot \int_{t-\frac{\delta}{2}}^{t+\frac{\delta}{2}} WC_{\Delta Y_r^j \Delta Y_r^j}(\tau) d\tau - \left| \int_{t-\frac{\delta}{2}}^{t+\frac{\delta}{2}} WC_{\Delta X_r^j \Delta Y_r^j}(\tau) d\tau \right|^2} \quad (8)$$

$$T_{zx}^j(t) = \frac{\int_{t-\frac{\delta}{2}}^{t+\frac{\delta}{2}} WC_{\Delta X_r^j \Delta Z_s^j}(\tau) d\tau \cdot \int_{t-\frac{\delta}{2}}^{t+\frac{\delta}{2}} WC_{\Delta Y_r^j \Delta Y_r^j}(\tau) d\tau - \int_{t-\frac{\delta}{2}}^{t+\frac{\delta}{2}} WC_{\Delta X_r^j \Delta Y_r^j}(\tau) d\tau \cdot \int_{t-\frac{\delta}{2}}^{t+\frac{\delta}{2}} WC_{\Delta Y_r^j \Delta Z_s^j}(\tau) d\tau}{\int_{t-\frac{\delta}{2}}^{t+\frac{\delta}{2}} WC_{\Delta X_r^j \Delta X_r^j}(\tau) d\tau \cdot \int_{t-\frac{\delta}{2}}^{t+\frac{\delta}{2}} WC_{\Delta Y_r^j \Delta Y_r^j}(\tau) d\tau - \left| \int_{t-\frac{\delta}{2}}^{t+\frac{\delta}{2}} WC_{\Delta X_r^j \Delta Y_r^j}(\tau) d\tau \right|^2} \quad (9)$$

$$T_{zy}^j(t) = \frac{\int_{t-\frac{\delta}{2}}^{t+\frac{\delta}{2}} WC_{\Delta Y_r^j \Delta Z_s^j}(\tau) d\tau \cdot \int_{t-\frac{\delta}{2}}^{t+\frac{\delta}{2}} WC_{\Delta X_r^j \Delta X_r^j}(\tau) d\tau - \int_{t-\frac{\delta}{2}}^{t+\frac{\delta}{2}} WC_{\Delta Y_r^j \Delta X_r^j}(\tau) d\tau \cdot \int_{t-\frac{\delta}{2}}^{t+\frac{\delta}{2}} WC_{\Delta X_r^j \Delta Z_s^j}(\tau) d\tau}{\int_{t-\frac{\delta}{2}}^{t+\frac{\delta}{2}} WC_{\Delta X_r^j \Delta X_r^j}(\tau) d\tau \cdot \int_{t-\frac{\delta}{2}}^{t+\frac{\delta}{2}} WC_{\Delta Y_r^j \Delta Y_r^j}(\tau) d\tau - \left| \int_{t-\frac{\delta}{2}}^{t+\frac{\delta}{2}} WC_{\Delta X_r^j \Delta Y_r^j}(\tau) d\tau \right|^2} \quad (10)$$

where

$$R_{\Delta X_s \Delta X_r}(t, f) = \frac{W_{\Delta X_s \Delta X_r}(t, f)}{\sqrt{W_{\Delta X_s \Delta X_s}(t, f) \cdot W_{\Delta X_r \Delta X_r}(t, f)}} \quad (20)$$

$$R_{\Delta X_s \Delta Y_r}(t, f) = \frac{W_{\Delta X_s \Delta Y_r}(t, f)}{\sqrt{W_{\Delta X_s \Delta X_s}(t, f) \cdot W_{\Delta Y_r \Delta Y_r}(t, f)}} \quad (21)$$

$$R_{\Delta X_r \Delta Y_r}(t, f) = \frac{W_{\Delta X_r \Delta Y_r}(t, f)}{\sqrt{W_{\Delta X_r \Delta X_r}(t, f) \cdot W_{\Delta Y_r \Delta Y_r}(t, f)}} \quad (22)$$

$$R_{\Delta Y_r \Delta X_r}(t, f) = \frac{W_{\Delta Y_r \Delta X_r}(t, f)}{\sqrt{W_{\Delta Y_r \Delta Y_r}(t, f) \cdot W_{\Delta X_r \Delta X_r}(t, f)}} \quad (23)$$

$W_{\Delta X_s \Delta X_r}(t, f)$ is calculated as follows:

$$W_{\Delta X_s \Delta X_r}(t, f) = \int_{t-\frac{\delta}{2}}^{t+\frac{\delta}{2}} \Delta X_s^j(\tau) \cdot \Delta X_r^j(\tau)^* d\tau \quad (24)$$

where $\Delta X_s^j(\tau)$ is the wavelet coefficient of ΔX_s at period j and time τ . The wavelet coefficient is obtained by using (12). $W_{\Delta X_s \Delta X_s}(t, f)$, $W_{\Delta X_r \Delta X_r}(t, f)$, $W_{\Delta X_s \Delta Y_r}(t, f)$, $W_{\Delta Y_r \Delta Y_r}(t, f)$, $W_{\Delta Y_r \Delta X_r}(t, f)$, and $W_{\Delta X_r \Delta Y_r}(t, f)$ are similar to those calculations of $W_{\Delta X_s \Delta X_r}(t, f)$. Similarly, the multivariate wavelet coherence coefficient of ΔY_s with ΔX_r and ΔY_r can be calculated as above, as well as ΔZ_s with ΔX_r and ΔY_r .

III. DATA

In this study, we use the Kakioka (KAK) Magnetic Observatory as a remote reference in computing interstation transfer functions of KYS stations at Boso Peninsula. The locations of all stations used in the study are shown in Fig. 3. Fig. 4(a), (c), and (e) illustrates the original data of geomagnetic variations of the observatory KYS (35.16°N and 140.15°E) and reference station KAK (36.23°N and 140.19°E), during a period at midnight on April 5, 2001 (JST). The sampling rate of data is 1 s.

The interstation transfer function can only be obtained by (1) when the external electromagnetic wave penetrates into the ground vertically as a plane wave [31]. Before the calculation, it is necessary to apply a high-pass filter to the raw signals. In accordance with previous studies [31], we apply a high-pass filter with a cutoff frequency of 940 s to the raw variations. Fig. 4(b), (d), and (f) shows the high-pass filtered of the components for each station. The horizontal components (ΔX and ΔY) of these two stations exhibit relatively similar variations, while the vertical components (ΔZ) display a phase difference.

To minimize artificial noises, the calculations are performed within the time interval of 2:00–4:00 on each selected day. Taking the horizontal magnetic field data of KYS and KAK stations as an example, Fig. 5 illustrates the multivariate wavelet coherences between the three components of KYS and the two horizontal components of KAK. $R_{(\Delta X_s, \Delta X_r, \Delta Y_r)}^2(t, f)$,

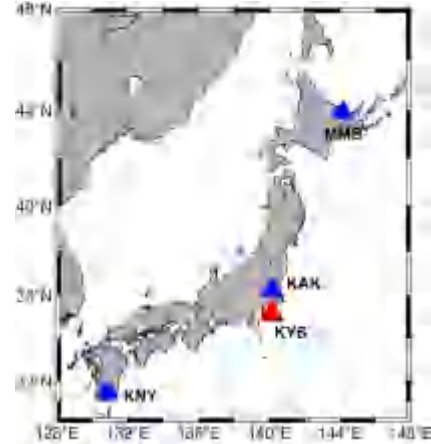


Fig. 3. Location of all the stations used.

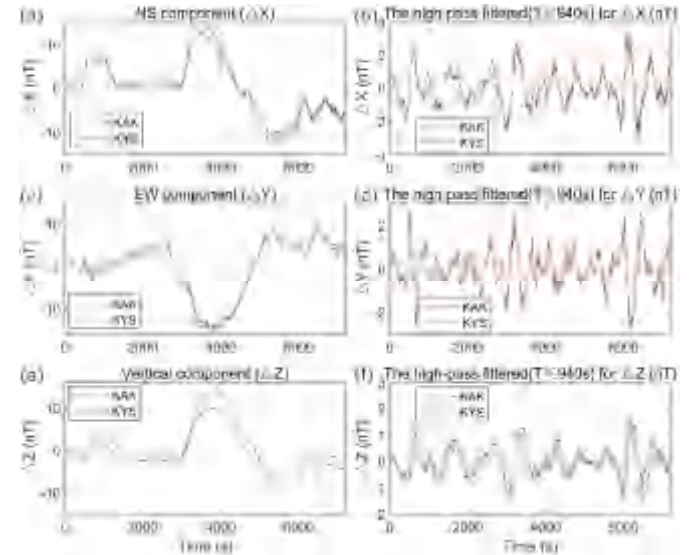


Fig. 4. Original and filtered data of geomagnetic variations for an interval of 02:00–04:00 on April 5, 2001 (JST) at KAK and KYS. (a) NS component (ΔX). (b) Filtered data for ΔX . (c) EW component (ΔY). (d) Filtered data for ΔY . (e) Vertical component (ΔZ). (f) Filtered data for ΔZ .

$R_{(\Delta Y_s, \Delta X_r, \Delta Y_r)}^2$, and $R_{(\Delta Z_s, \Delta X_r, \Delta Y_r)}^2$ are generally over 0.9 for frequencies above 100 s, indicating a high signal-to-noise ratio (SNR) in the lower frequency range. It is suggested that there is high data quality for the interstation transfer function calculations in the lower frequency signals. The coherence exhibits variations over time in the relatively higher frequency signals, such as below 50 s.

As the period becomes shorter, overall coherence decreases, which indicates a higher noise level in the higher frequency signals. Larger noise levels typically lead to greater errors in transfer function calculations. As shown in Fig. 6, an example is provided of the error plot for the mean and standard deviation of transfer functions for a 10-s period on a particular

$$R_{(\Delta X_s, \Delta X_r, \Delta Y_r)}^2(t, f) = \frac{R_{\Delta X_s \Delta X_r}^2(t, f) + R_{\Delta X_s \Delta Y_r}^2(t, f) - 2\text{Re}(R_{\Delta X_s \Delta X_r}(t, f) \cdot R_{\Delta X_s \Delta Y_r}^*(t, f) \cdot R_{\Delta Y_r \Delta X_r}^*(t, f))}{1 - R_{\Delta X_r \Delta Y_r}^2(t, f)} \quad (16)$$

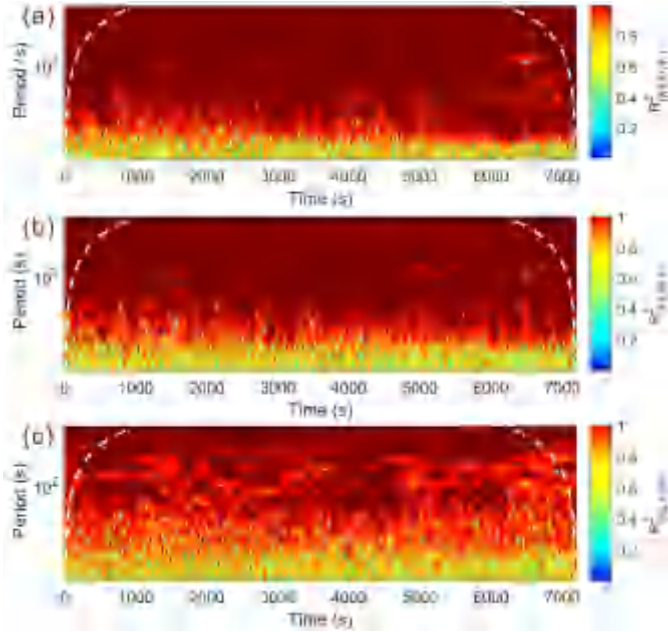


Fig. 5. Coherence between each component of KYS and horizontal components of KAK. (a) $R^2_{(\Delta X_s, \Delta X_r, \Delta Y_r)}$. (b) $R^2_{(\Delta Y_s, \Delta X_r, \Delta Y_r)}$. (c) $R^2_{(\Delta Z_s, \Delta X_r, \Delta Y_r)}$.

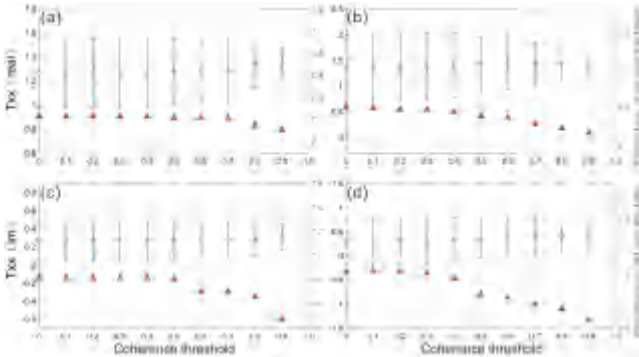


Fig. 6. Mean and standard deviations of the interstation transfer function at different multivariate coherence coefficient thresholds for an interval of April 5, 2001 (JST). The red triangle for the right vertical coordinate is the percentage of the deviation over the mean value. (a) T_{xx} (real). (b) T_{yy} (real). (c) T_{xx} (imaginary). (d) T_{yy} (imaginary).

day, where different coherence threshold values are selected. Notably, the standard deviation of the transfer function values significantly decreases when the coherence threshold reaches 0.9. In this study, a coherence threshold of 0.95 is chosen, ensuring accurate estimation of transfer functions. For a specific period, we calculate the mean of transfer function results that reach the 0.95 coherence threshold within all windows and take the mean value as the interstation transfer function result on the given day.

IV. RESULTS

The frequency response of a system is the essence of the interstation transfer function relationship, where two horizontal components are from a reference station as inputs and components are from an observatory as outputs. The coherences between observatory and reference station show high value when input signals from Earth's spatial field sources are

strong and artificial noise is low. Therefore, this study utilizes the days with $K_p \geq 5$ between May 2000 and April 2010 for the estimation of interstation transfer functions and selects data from the midnight time period, to ensure a high SNR in the raw data. Transfer function results for different frequencies are obtained by averaging the values from windows with a multivariate coherence reaching 0.95 for that frequency on a given day. The overall result for interstation transfer functions is derived by averaging all days. To be specific, we optimize the coherence calculation and window length design, as described in Section II. Fig. 7 illustrates the obtained interstation transfer function values for KAK-KYS by using the improved method proposed in this study. The solid blue circles and hollow red circles represent the real and imaginary parts, respectively. The real and imaginary parts of the six interstation transfer function values calculated by this method show good continuity and stability across different periods, indicating the accuracy of the method in practice. By comparing the six transfer function values, it can be seen that the real and imaginary parts of T_{xy} and T_{yx} are both near 0, while those of T_{xx} and T_{yy} are between 0 and 2. It is suggested a higher correlation between the horizontal components ΔX_s and ΔX_r , and a lower correlation between the horizontal components ΔY_s and ΔX_r . Similarly, the horizontal component ΔY_s of the observatory is more correlated with the horizontal component ΔY_r of the reference station and less correlated with the horizontal component ΔX_r . In addition, compared to the short periods, both the vertical components T_{zx} and T_{zy} exhibit changes at long periods, indicating a correlation between the vertical component ΔZ_s of the observatory and both horizontal components of the reference station. The transfer functions vary with the change of period, which might reflect variations in different depths.

Fig. 8 shows the three observed and estimated components of the geomagnetic field variations at the KAK and KYS stations during a 30-min period on a specific day (JST April 5, 2001) with $K_p \geq 5$. This day had significant geomagnetic activities and the previous studies have suggested that there was tram interference at certain times [31]. In Fig. 8(a), the blue and red lines represent the high-pass filtered (a cutoff frequency of 940 s) data of observed variations in the X component for KAK and KYS stations, respectively. The purple lines are the estimated values for KYS, which is obtained by the interstation transfer function based on the two observed horizontal components at reference station KAK. To facilitate the comparison, the blue and red lines are shifted by 2 and 1 nT during plotting, respectively, providing a clearer contrast in the magnetic field changes at the same time. The trends of the observed values at KAK and KYS stations are generally consistent. Both stations appear low-frequency signals (about 300-s periods) with an amplitude of 2 nT at 500–800 s, as well as noticeable geomagnetic pulsations around 1000 s. In addition, synchronous signals with similar periods can be observed between 1000 and 1800 s, suggesting simultaneous influences from external spatial sources on both stations during this time period. In Fig. 8(b), the residuals between the observed and estimated values for KYS are shown, with the overall variations near 0, indicating that the estimated values are basically the same as the observed values.

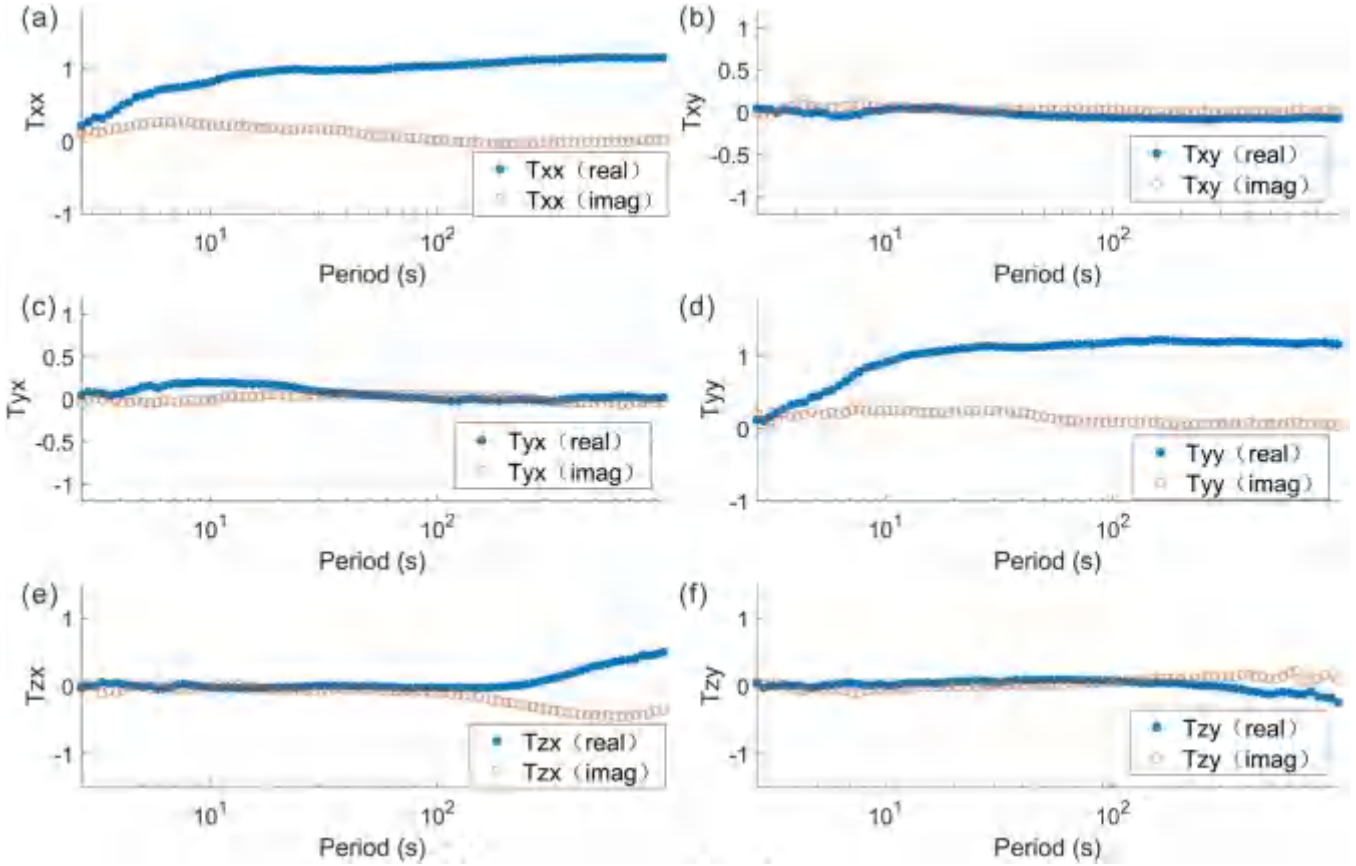


Fig. 7. Estimated interstation transfer functions between KAK and KYS stations. (a) T_{xx} . (b) T_{xy} . (c) T_{yx} . (d) T_{yy} . (e) T_{zx} . (f) T_{zy} . Solid and hollow circles indicate the real and imaginary parts of interstation transfer functions, respectively. Interstation transfer functions are calculated using midnight time data with $K_p \geq 5$ days.

In particular, the amplitude of the noticeable geomagnetic pulsation signal at 1000 s is approximatively reduced to zero in the residuals, demonstrating the effective recovery of spatial field sources by the estimated values. Moreover, a weak local anomaly with an amplitude of about 0.1 nT is identified around 400 s in the residuals, indicating the high precision of the method. Later, we apply the same steps to obtain the estimated values for the Y component of the KYS station during the time, as shown in Fig. 8(c). Similar to the observed values for the X component in Fig. 8(a), both stations exhibit noticeable short-period geomagnetic pulsations around 1000 s and synchronous variations signals with similar periods between 1000 and 1800 s. In Fig. 8(d), the black lines are the residuals between the observed and estimated values for KYS in the Y component. The residuals exhibit variations near 0, indicating a substantial agreement between the estimated and actual observed values. Specifically, the amplitude of the noticeable geomagnetic pulsation signal disappears at 1000 s in the residuals. The horizontal component results show that the residuals eliminate the spatial field source signals effectively, including geomagnetic pulsations.

The observed and estimated values for the vertical components (Z components) of KYS are presented in Fig. 8(e). In contrast to the horizontal X and Y components, the geomagnetic pulsation signals in the vertical component are relatively small, for example, the distinct geomagnetic pulsation signal

observed at 1000 s is absent for both KAK and KYS stations in the vertical component. It is suggested that the assumption of negligible disturbances in the vertical component under plane wave incidence conditions is valid. As for the phase difference of vertical components between the KAK and KYS stations, the real and imaginary parts of interstation transfer function values contain phase's information, allowing for the transfer of phase difference. The purple lines in Fig. 8(e) show the estimated values for KYS, whose phase is consistent with the phase of observed values, indicating that the phase difference between the two stations can be recovered through the interstation transfer function.

Fig. 8(f) displays the residuals between the observed and estimated values for the Z component of KYS, revealing conspicuous anomalies with amplitudes within 1 nT. This signal corresponds to noise generated when a tram passes near the KYS station [31]. The significant values in the residuals indicate that the vertical component mainly reflects local anomalies near the KYS station.

These results strongly underscore the capability of estimating background field variations in the Z component of the observatory by the proposed method, including phase difference. The residuals between observed values and estimated values reflect local signal variations near the station, which strongly affirm the accuracy and reliability of the interstation transfer function calculations. Based on the above

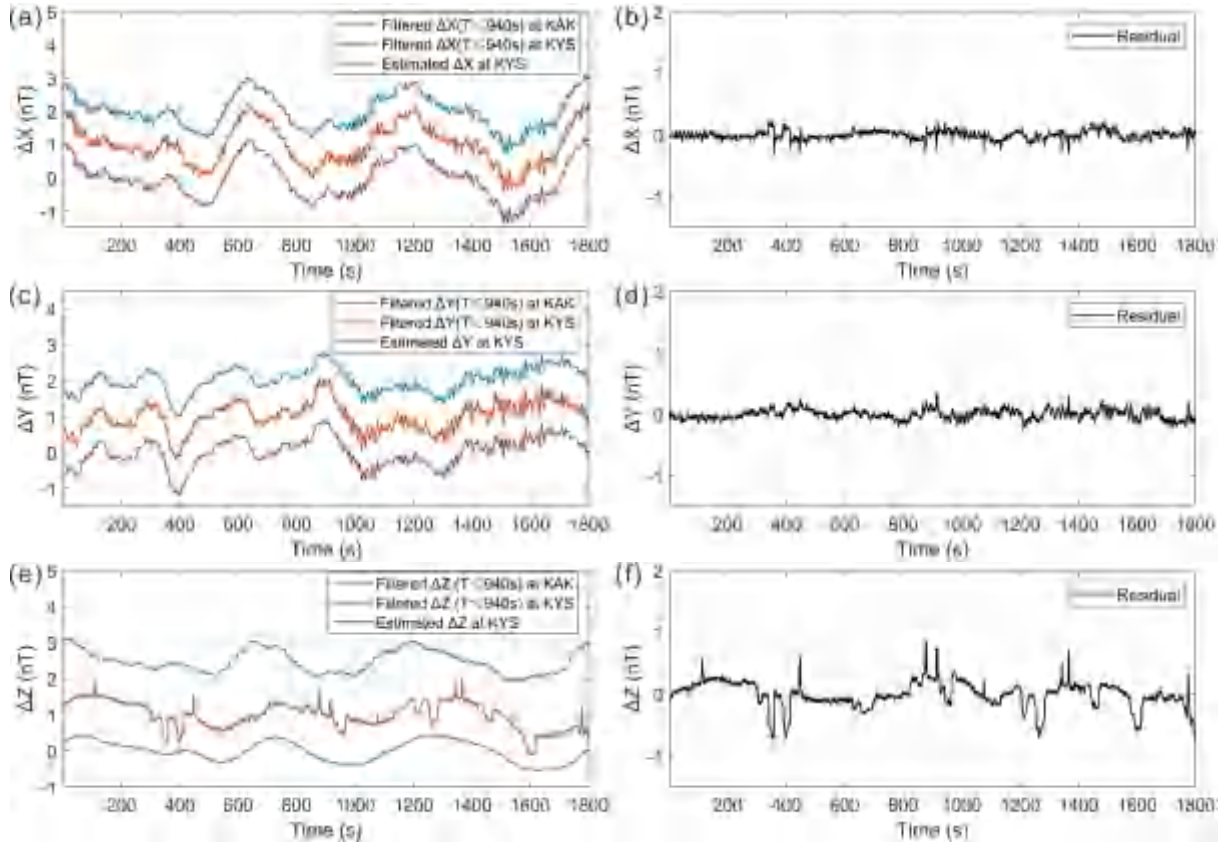


Fig. 8. Experimental results of the global signal estimation at KYS station based on KAK. (a) Filtered data at KAK, KYS, and estimated data at KYS in NS component (ΔX). (b) Residual between estimated and filtered data at KYS in NS component (ΔX). (c) Filtered data at KAK, KYS, and estimated data at KYS in EW component (ΔY). (d) Residual at KYS in the EW component (ΔY). (e) Filtered data at KAK, KYS, and estimated data at KYS in vertical component (ΔZ). (f) Residual at KYS in vertical component (ΔZ). Note that the blue and red lines in (a), (c), and (e) are shifted by 2 and 1 nT.

results, it can be seen that the proposed method based on multivariate wavelet coherence can recover the natural background signal variations of three components, so as to extract local ultralow-frequency geomagnetic signal variations at the observatory.

In order to verify the effectiveness of eliminating the global signal (global signal reduction) by the interstation function, we calculate the correlation of X and Y components for geomagnetic field variations between KAK and KYS stations. Fig. 9(a) and (c) shows the NS and EW components of the original data between KAK and KYS stations over 2 h in the period of 02:00–04:00 (JST) on April 5, 2001, respectively. Fig. 9(b) and (d) shows the NS and EW components of the between KAK raw data and residual of KYS station, respectively. The correlation coefficient of the original data in X and Y components is high, about 0.99 and 0.97, respectively. On the other hand, the correlation coefficient between original data at KAK and residuals at KYS is reduced by about 0.03. This implies that the global natural signals from the external sources in X and Y components of KYS station are eliminated satisfactorily.

V. DISCUSSION

A. Advantage of the Proposed Method

Among the methods of extracting the local signals from the global natural signals, the interstation transfer function

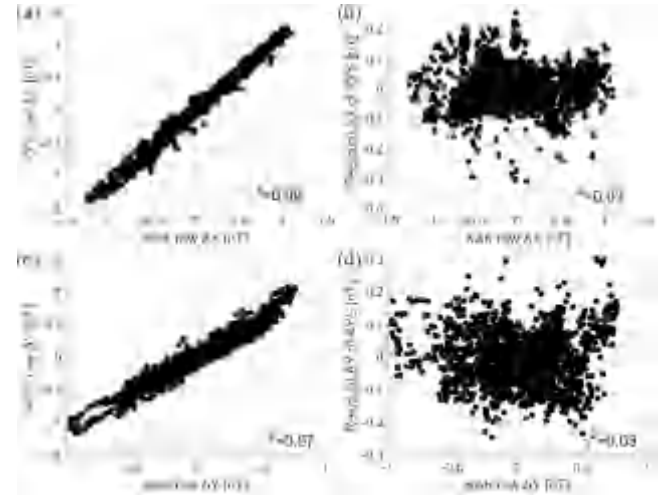


Fig. 9. Correlation of NS (ΔX) and EW (ΔY) component for geomagnetic field variations between KYS and KAK stations. The data period is 02:00–04:00 on April 5, 2001 (JST). (a) Raw data of KYS and KAK in X component. (b) Residual after global signal reduction of X component in KYS and raw KAK data. (c) Raw data of KYS and KAK in Y component. (d) Residual of Y component in KYS and raw KAK data.

method can recover the waveform of the background field of the observatory, so as to analyze the local geomagnetic signals more quantitatively. However, the previous transfer function method lacks strict multivariate coherent calculation, and the

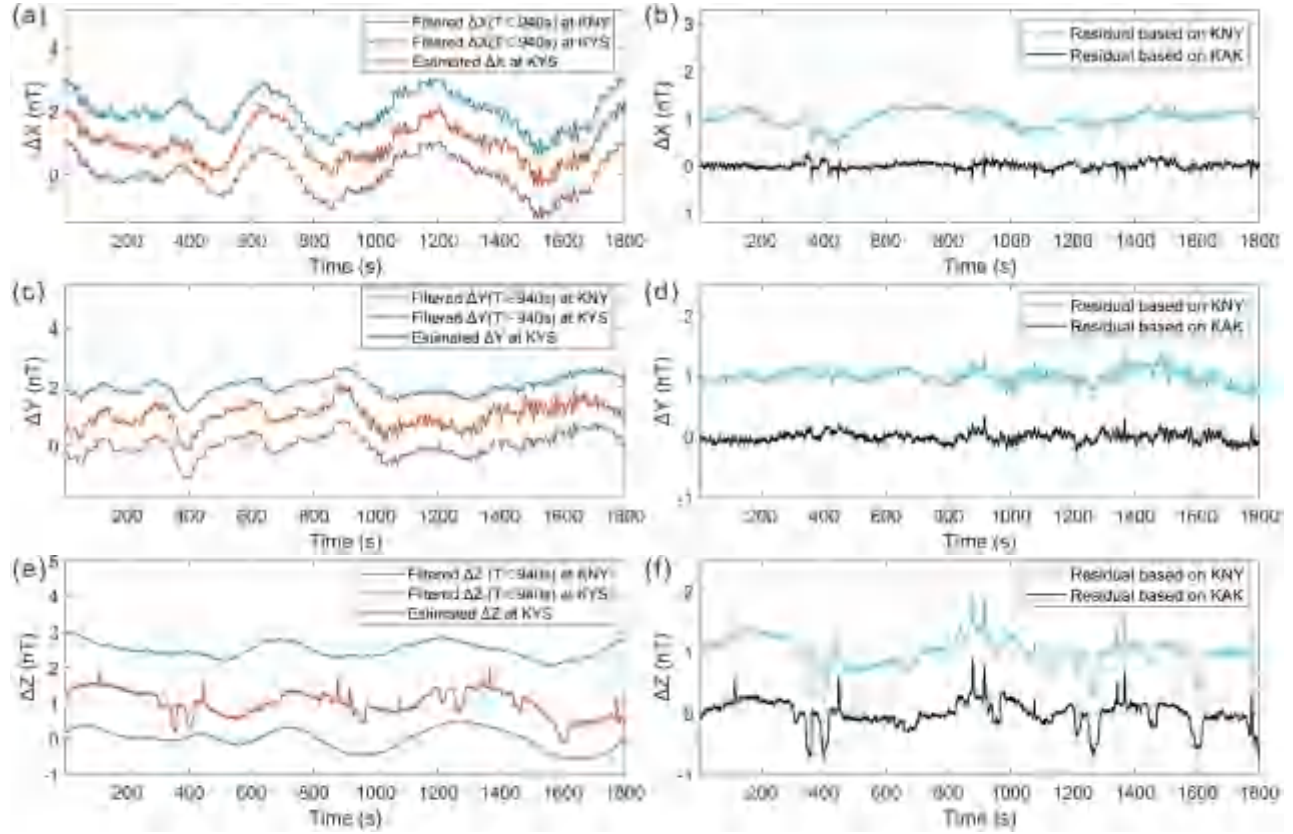


Fig. 10. Experimental results of the global signal estimation at KYS station based on KNY. Filtered data at KNY, KYS, and estimated data at KYS in (a) NS component (ΔX), (c) EW component (ΔY), and (e) vertical component (ΔZ). The residual between estimated and filtered data at KYS in (b) NS component (ΔX), (d) EW component (ΔY), and (f) vertical component (ΔZ). Note that the blue and red lines in (a), (c), and (e) are shifted by 2 and 1 nT, and the blue lines in (b), (d), and (f) are shifted by 1 nT.

window lengths for different period signals were too rough to be divided, resulting in a small number of effective sample data and low calculation accuracy [24]. In this article, we develop an interstation transfer function method based on multivariate wavelet coherence, to improve the accuracy of interstation transfer function. This method calculates multivariate wavelet coherence using observed data directly, employing a coherence threshold to filter high SNR data. A novel window length function is proposed, enabling adaptive selection of calculation time window lengths for different periods' transfer functions. The method addresses shortcomings of previous algorithms, such as coherence calculation and coarse window divisions, thereby improving the stability and precision of transfer function calculations.

Empirical validation with real data demonstrates the effectiveness of the proposed method, highlighting its advantages. External sources of magnetic field signals are accurately computed by utilizing the proposed interstation transfer function methods, including the horizontal X and Y components and the vertical Z component of the observatory. This enables high-precision identification and extraction of local magnetic field disturbances at the observatory. In addition, during the time with high artificial noise, the method can identify tram signals, so it might also be used for the detection of metallic targets. Furthermore, it can be utilized to establish high-precision time-varying geomagnetic field models

regionally. After obtaining the waveform of local geomagnetic signals at the observatory, machine learning and other intelligent algorithms can be introduced for pattern recognition of geomagnetic signal waveforms in the future, in which the extracted waveform can provide training set samples for intelligent recognition.

B. Comparison of Reference Station

The first step in the calculation of transfer functions is to select an appropriate reference station. A reference station with high-quality, complete data, and high SNR observations serves as the basis for accurate interstation transfer function calculation and analysis of anomalous signals at the observatory. Therefore, in this study, in order to verify and confirm the robustness of the method, two international reference stations are chosen as reference stations to compare the results of KAK, including Kanoya (KNY) (31.42°N and 130.88°E) and Memanbetsu (MMB) (43.91°N and 144.18°E).

KNY is located in the lower latitude region of southwestern Japan, while MMB is situated in the higher latitude region of northeastern Japan. Figs. 10 and 11 show the estimated results that are obtained by using these two reference stations, respectively, and their comparison with those of using KAK station. The residual based on KNY and MMB is shifted by

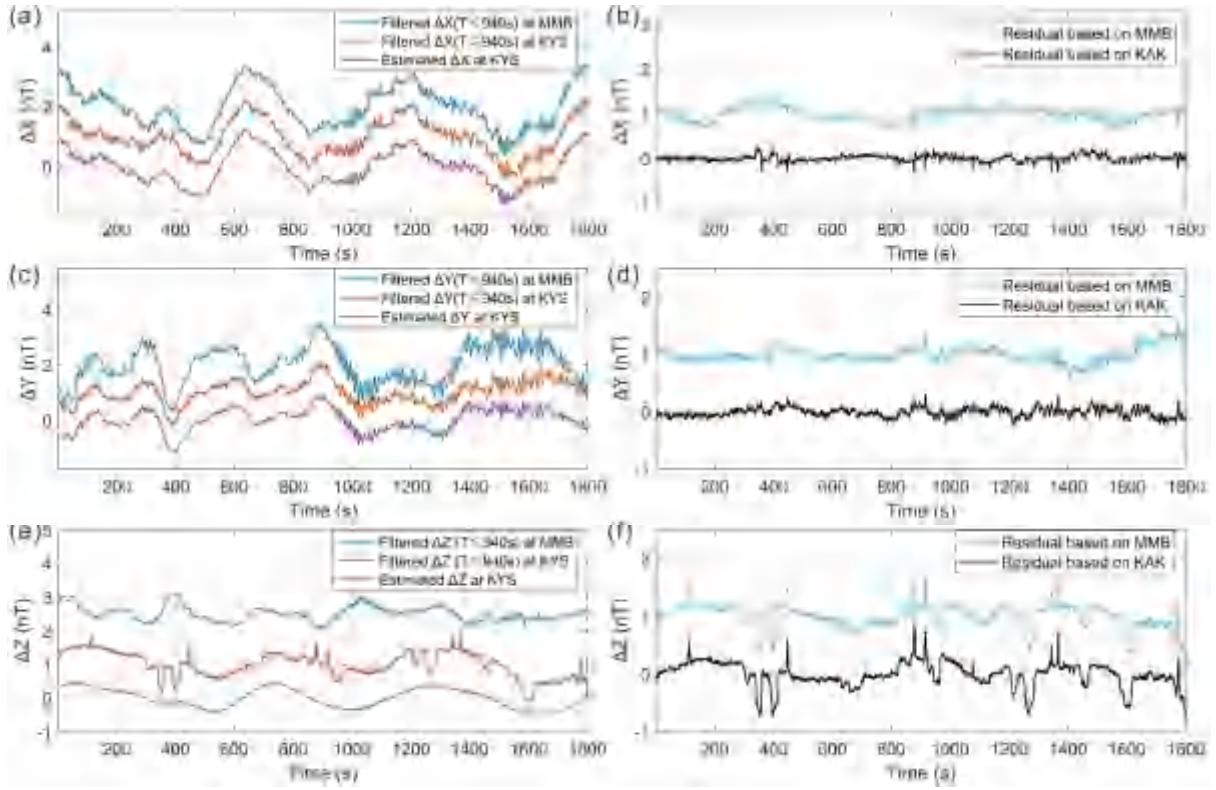


Fig. 11. Experimental results of the global signal estimation at KYS station based on MMB. Filtered data at KNY, KYS, and estimated data at KYS in (a) NS component (ΔX), (c) EW component (ΔY), and (e) vertical component (ΔZ). The residual between estimated and filtered data at KYS in (b) NS component (ΔX), (d) EW component (ΔY), and (f) vertical component (ΔZ). Note that the blue and red lines in (a), (c), and (e) are shifted by 2 and 1 nT, and the blue lines in (b), (d), and (f) are shifted by 1 nT.

1 nT during plotting, providing a contrast with those based on KAK at the same time.

For the observed data, there are certain differences between observatory KYS and two reference stations in the signal amplitudes. Particularly, in the presence of geomagnetic pulsation signals, the amplitude of the Y component's spatial field source signal from KNY is smaller, while MMB records a larger amplitude of spatial field source signal changes compared to KYS, resulting in the difference of estimated KYS station. In addition, some geomagnetic pulsation signals are recorded in the vertical Z component of MMB, suggesting that the assumption of negligible disturbances in the vertical component under plane wave incidence conditions may not fully satisfy this station. The results of estimated values are largely consistent with those by the KAK station, including background spatial field sources for the X and Y components of both reference stations. The amplitude of geomagnetic pulsations in the residuals is basically eliminated. Besides, the vertical Z component, which exhibits phase differences, is accurately estimated through the interstation transfer function for the two references. In general, due to the distinct longitudes and latitudes of the stations, there are notable differences in spatial field sources for KNY, MMB, and KAK stations. As can be seen from Figs. 10 and 11, there are still some long-period signals in the residuals obtained by using KNY and MMB as reference stations because the consistency of external field sources of the two stations is not so good with observatory in the long-period signals. In order to ensure better

external source consistency, we need to use a closer reference station. Furthermore, being located in a higher latitude region, MMB may be influenced by current systems in the polar region. Therefore, it is more reasonable to select KAK as the reference station, whose position and the spatial field sources are closer to the observatory KYS. Recently, a study found that only when using two stations close to the observatory as reference stations, identifying ULF anomaly signals during seismogenic periods is available [30]. This study also provides evidence for reasonable of choosing KAK as a reference station.

VI. CONCLUSION

In summary, we develop an interstation transfer function method based on multivariate wavelet coherence to extract ultralow-frequency geomagnetic signals. Our method calculates multivariate wavelet coherence using observed data directly and enables adaptive selection of time window lengths for different periods, thereby improving the stability and precision of transfer function calculations. Empirical validation with real data demonstrates that external sources of magnetic field signals are accurately estimated by the proposed interstation transfer function methods, including the horizontal and vertical components of the observatory. We compare the results for using different reference stations, confirming the robustness of the method. The proposed method enables high-precision identification and extraction of local magnetic

field disturbances at the observatory, and it can be useful in seismo-electromagnetic signal identification and extraction in the future.

ACKNOWLEDGMENT

The authors would like to thank Japan Meteorological Agency for providing geomagnetic data and ISGI Collaborating Institute GFZ Potsdam, Germany, for providing geomagnetic Kp indices. They also thank the editor and five anonymous reviewers for their suggestions and comments.

REFERENCES

- [1] M. J. S. Johnston, "Review of electric and magnetic fields accompanying seismic and volcanic activity," *Surv. Geophys.*, vol. 18, no. 5, pp. 441–475, Sep. 1997.
- [2] S. Uyeda, T. Nagao, and M. Kamogawa, "Short-term earthquake prediction: Current status of seismo-electromagnetics," *Tectonophysics*, vol. 470, nos. 3–4, pp. 205–213, May 2009.
- [3] K. Hattori, "ULF geomagnetic changes associated with large earthquakes," *Terr. Atmos. Ocean. Sci.*, vol. 15, no. 3, p. 329, 2004.
- [4] P. Han et al., "Statistical analysis of ULF seismomagnetic phenomena at Kakioka, Japan, during 2001–2010," *J. Geophys. Res., Space Phys.*, vol. 119, no. 6, pp. 4998–5011, Jun. 2014.
- [5] Q. Huang, P. Han, K. Hattori, and H. Ren, "Electromagnetic signals associated with earthquakes," *Seismoelectric Explor.*, vol. 2020, pp. 415–436, Jul. 2020.
- [6] M. Hayakawa, J. Y. Liu, K. Hattori, and L. Telesca, "Electromagnetic phenomena associated with earthquakes and volcanoes preface," *Phys. Chem. Earth*, vol. 34, nos. 6–7, pp. 341–342, 2009.
- [7] J. Y. Liu et al., "The vertical propagation of disturbances triggered by seismic waves of the 11 March 2011 M9.0 Tohoku earthquake over Taiwan," *Geophys. Res. Lett.*, vol. 43, no. 4, pp. 1759–1765, Feb. 2016.
- [8] J. Zhang et al., "Oscillations of the ionosphere caused by the 2022 Tonga volcanic eruption observed with SuperDARN radars," *Geophys. Res. Lett.*, vol. 49, no. 20, pp. 1–29, Oct. 2022.
- [9] J. C. Dunson, T. E. Bleier, S. Roth, J. Heraud, C. H. Alvarez, and A. Lira, "The pulse azimuth effect as seen in induction coil magnetometers located in California and Peru 2007–2010, and its possible association with earthquakes," *Natural Hazards Earth Syst. Sci.*, vol. 11, no. 7, pp. 2085–2105, Jul. 2011.
- [10] Q. Huang, "Rethinking earthquake-related DC-ULF electromagnetic phenomena: Towards a physics-based approach," *Natural Hazards Earth Syst. Sci.*, vol. 11, no. 11, pp. 2941–2949, Nov. 2011.
- [11] P. Varotsos, K. Alexopoulos, K. Nomicos, and M. Lazaridou, "Earthquake prediction and electric signals," *Nature*, vol. 322, no. 6075, pp. 120–120, Jul. 1986.
- [12] V. S. Nicholas et al., "Seismic electric signals in seismic prone areas," *Earthq. Sci.*, vol. 31, no. 1, pp. 44–51, 2018.
- [13] E. S. Skordas and N. V. Sarlis, "On the anomalous changes of seismicity and geomagnetic field prior to the 2011 9.0 Tohoku earthquake," *J. Asian Earth Sci.*, vol. 80, pp. 161–164, Feb. 2014.
- [14] S. Warden, T. Bleier, and K. Kappler, "Long term air ion monitoring in search of pre-earthquake signals," *J. Atmos. Solar-Terrestrial Phys.*, vol. 186, pp. 47–60, May 2019.
- [15] K. N. Kappler, D. D. Schneider, L. S. MacLean, T. E. Bleier, and J. J. Lemon, "An algorithmic framework for investigating the temporal relationship of magnetic field pulses and earthquakes applied to California," *Comput. Geosci.*, vol. 133, Dec. 2019, Art. no. 104317.
- [16] W. D. Heavlin et al., "Case-Control study on a decade of ground-based magnetometers in California reveals modest signal 24–72 hr prior to earthquakes," *J. Geophys. Res. Solid Earth*, vol. 127, no. 10, pp. 1–22, Oct. 2022.
- [17] T. Nagao et al., "Electromagnetic anomalies associated with 1995 Kobe earthquake," *J. Geodynamics*, vol. 33, nos. 4–5, pp. 401–411, May 2002.
- [18] A. De Santis et al., "Precursory worldwide signatures of earthquake occurrences on swarm satellite data," *Sci. Rep.*, vol. 9, no. 1, pp. 1–20, Dec. 2019.
- [19] M. Fan et al., "Exploration of the 2021 mw 7.3 maduo earthquake by fusing the electron density and magnetic field data of swarm satellites," *IEEE Trans. Geosci. Remote Sens.*, vol. 62, no. 1, pp. 1–24, Aug. 2021.
- [20] A. Bernardi, A. C. Fraser-Smith, P. R. McGill, and O. G. Villard, "ULF magnetic field measurements near the epicenter of the ms 7.1 loma prieta earthquake," *Phys. Earth Planet. Interiors*, vol. 68, nos. 1–2, pp. 45–63, Aug. 1991.
- [21] Y. A. Kopytenko, T. G. Matiashvili, P. M. Voronov, E. A. Kopytenko, and O. A. Molchanov, "Detection of ultra-low-frequency emissions connected with the spitak earthquake and its aftershock activity, based on geomagnetic pulsations data at dusheti and vardzia observatories," *Phys. Earth Planet. Interiors*, vol. 77, nos. 1–2, pp. 85–95, Apr. 1993.
- [22] M. Hayakawa, R. Kawate, O. A. Molchanov, and K. Yumoto, "Results of ultra-low-frequency magnetic field measurements during the Guam earthquake of 8 August 1993," *Geophys. Res. Lett.*, vol. 23, no. 3, pp. 241–244, Feb. 1996.
- [23] S. Uyeda et al., "Electric and magnetic phenomena observed before the volcano-seismic activity in 2000 in the izu island region, Japan," *Proc. Nat. Acad. Sci. USA*, vol. 99, no. 11, pp. 7352–7355, May 2002.
- [24] A. Serita, K. Hattori, C. Yoshino, M. Hayakawa, and N. Isezaki, "Principal component analysis and singular spectrum analysis of ULF geomagnetic data associated with earthquakes," *Natural Hazards Earth Syst. Sci.*, vol. 5, no. 5, pp. 685–689, Sep. 2005.
- [25] S. Wen et al., "Magnetic storm free ULF analysis in relation with earthquakes in Taiwan," *Natural Hazards Earth Syst. Sci.*, vol. 12, no. 5, pp. 1747–1754, May 2012.
- [26] K. Hattori, A. Serita, C. Yoshino, M. Hayakawa, and N. Isezaki, "Singular spectral analysis and principal component analysis for signal discrimination of ULF geomagnetic data associated with 2000 izu island earthquake swarm," *Phys. Chem. Earth, Parts A/B/C*, vol. 31, nos. 4–9, pp. 281–291, Jan. 2006.
- [27] K. Hattori, P. Han, C. Yoshino, F. Febriani, H. Yamaguchi, and C.-H. Chen, "Investigation of ULF seismo-magnetic phenomena in kanto, Japan during 2000–2010: Case studies and statistical studies," *Surveys Geophysics*, vol. 34, no. 3, pp. 293–316, May 2013.
- [28] P. Han, K. Hattori, J. Zhuang, C.-H. Chen, J.-Y. Liu, and S. Yoshida, "Evaluation of ULF seismo-magnetic phenomena in Kakioka, Japan by using Molchan's error diagram," *Geophys. J. Int.*, vol. 208, no. 1, pp. 482–490, Jan. 2017.
- [29] P. Han et al., "Assessing the potential earthquake precursory information in ULF magnetic data recorded in kanto, Japan during 2000–2010: Distance and magnitude dependences," *Entropy*, vol. 22, no. 8, p. 859, Aug. 2020.
- [30] J. Xue, Q. Huang, S. Wu, and L. Zhao, "Detection of ULF geomagnetic anomalies prior to the tohoku-oki earthquake by the multireference station method," *IEEE Trans. Geosci. Remote Sens.*, vol. 62, 2024, Art. no. 5910009.
- [31] M. Harada, K. Hattori, and N. Isezaki, "Transfer function approach to signal discrimination of ULF geomagnetic data," *Phys. Chem. Earth, Parts A/B/C*, vol. 29, nos. 4–9, pp. 409–417, Jan. 2004.
- [32] K. Hattori, Y. Akinaga, M. Hayakawa, K. Yumoto, T. Nagao, and S. Uyeda, "ULF-magnetic anomaly preceding the 1997 Kagoshima earthquakes," in *Seismo-Electromagnetics: Lithosphere. Atmosphere. Ionosphere Coupling*, M. Hayakawa and O. A. Malchanov, Eds., Tokyo, Japan: Terra Scientific Publishing Company, 2002, pp. 19–28.
- [33] M. Hayakawa, T. Itoh, K. Hattori, and K. Yumoto, "ULF electromagnetic precursors for an earthquake at biak, Indonesia on February 17, 1996," *Geophys. Res. Lett.*, vol. 27, no. 10, pp. 1531–1534, May 2000.
- [34] K. Gotoh, K. Hattori, and M. Hayakawa, "Identification of ULF emissions for Izu islands earthquakes," in *Proc. Asia-Pacific Conf. Environ. Electromagn.*, 2000, pp. 217–220.
- [35] A. A. Akyol, O. Arikhan, and F. Arikhan, "A machine learning-based detection of earthquake precursors using ionospheric data," *Radio Sci.*, vol. 55, no. 11, pp. 1–21, Nov. 2020.
- [36] J. Xue, Q. Huang, S. Wu, and T. Nagao, "LSTM-autoencoder network for the detection of seismic electric signals," *IEEE Trans. Geosci. Remote Sens.*, vol. 60, 2022, Art. no. 5917012.
- [37] J. Xue, S. Wu, Q. Huang, L. Zhao, N. V. Sarlis, and P. A. Varotsos, "RASE: A real-time automatic search engine for anomalous seismic electric signals in geoelectric data," *IEEE Trans. Geosci. Remote Sens.*, vol. 61, 2023, Art. no. 5905911.

- [38] S. Furwara and H. Tou, "Geomagnetic transfer functions in Japan obtained by first order geomagnetic survey," *J. Geomagnetism Geoelectricity*, vol. 48, no. 8, pp. 1071–1101, 1996.
- [39] E. K. W. Ng and J. C. L. Chan, "Geophysical applications of partial wavelet coherence and multiple wavelet coherence," *J. Atmos. Ocean. Technol.*, vol. 29, no. 12, pp. 1845–1853, Dec. 2012.



Hongyan Chen received the B.S. degree in geoinformation science and technology and the M.S. degree in geodetection and information technology from the Ocean University of China, Qingdao, China, in 2016 and 2019, respectively, and the Ph.D. degree in physics from the Southern University of Science and Technology, Shenzhen, China, in 2023.

She is currently a Post-Doctoral Fellow with the Department of Earth and Space Sciences, Southern University of Science and Technology, Shenzhen.

Her research interests include seismo-electromagnetics, seismic precursor analysis, and signal processing.

Dr. Chen is a member of the Shenzhen Key Laboratory of Deep Offshore Oil and Gas Exploration Technology and Guangdong Provincial Key Laboratory of Geophysical High-Resolution Imaging Technology, China. She received the Outstanding Youth Science and Technology Award of the Seismological Society of China and the Outstanding Graduates (Ph.D.) Award of the Southern University of Science and Technology.



Peng Han (Member, IEEE) received the B.S. degree in geophysics from the School of Earth and Space Sciences, Peking University, Beijing, China, in 2006, the M.S. degree in geophysics from the Institute of Geophysics, China Earthquake Administration, Beijing, in 2009, and the Ph.D. degree in geophysics from Chiba University, Chiba, Japan, in 2013.

He was a Post-Doctoral Research Fellow with Chiba University and the Institute of Statistical Mathematics, Tachikawa, Japan, from 2013 to 2017. He is currently an Associate Professor with the Department of Earth and Space Sciences, Southern University of Science and Technology, Shenzhen, China. His research fields include signal processing, seismo-electromagnetics, statistical seismology, and natural hazards.

Dr. Han is a Core Member of Shenzhen Key Laboratory of Deep Offshore Oil and Gas Exploration Technology and Guangdong Provincial Key Laboratory of Geophysical High-Resolution Imaging Technology, China. He received the Outstanding Presentation Award of the Society of Atmospheric Electricity of Japan, the Excellent Paper Award of the Institute of Electrical Engineers of Japan, and the Outstanding Graduates (Ph.D.) Award of the Faculty of Science, Chiba University.



Katsumi Hattori (Member, IEEE) received the Ph.D. degree in electrical and electronics engineering from Nagoya University, Nagoya, Japan, in 1992.

Since 2007, he has been a Professor with the Graduate School of Science, Chiba University. He is currently the Vice President of Chiba University. His current research interests include electromagnetic approaches to mitigate natural hazards and to forecast in crustal disasters, such as earthquakes, volcano eruptions, and landslides.